RSC Advances

ROYAL SOCIETY OF CHEMISTRY

www.rsc.org/advances

Table of Contents

Synthesis of small Fe_2O_3 nanocubes and their enhanced water vapour adsorption-desorption properties

Feng Cao[a], Duanyang Li[a], Ruiping Deng[b], Lijian Huang[b], Daocheng Pan[b], Jianmin Wang[a], Song Li[a], Gaowu Qin*[a]

[a]Key Laboratory for Anisotropy and Texture of Materials (Ministry of Education), Northeastern University, Shenyang 110819, China.

[b]State Key Laboratory of Rare Earth Resource Utilization, Changchun Institute of Applied Chemistry, Chinese Academy of Sciences, Changchun 130022, China

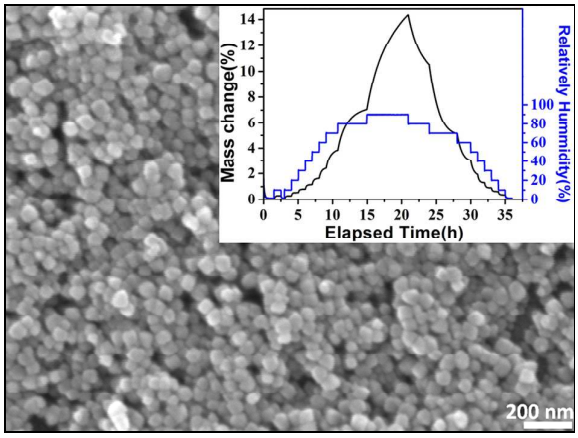

Uniform ordered Fe_2O_3 nanocubes showed an excellent humidity-controlling ability, due to their appropriate pore size distribution nearby condensation critical radius.

Journal Name

COMMUNICATION

Synthesis of small Fe_2O_3 nanocubes and their enhanced water vapour adsorption-desorption properties

Received 00th January 20xx,
Accepted 00th January 20xx

DOI: 10.1039/x0xx00000x

www.rsc.org/

Feng Cao,[a] Duanyang Li,[a] Ruiping Deng,[b] Lijian Huang,[b] Daocheng Pan,[b] Jianmin Wang,[a] Song Li,[a] and Gaowu Qin*[a]

It is of great importance to develop humidity-buffering materials and thus to improve indoor environment. Uniform Fe_2O_3 nanocubes with an average pore size distribution of 8.48 nm exhibit superior water adsorption-desorption ability, arise from the appropriate pore size distribution around condensation critical radius. This finding can provide a novel strategy to design and preparation of new humidity-buffering nanomaterials.

Water adsorption technologies have attracted a tremendous amount of interests due to their extensive applications in construction field, pharmaceutical processing, food industry, microelectronics, and so on. Examples include desiccant dehumidifier, the adsorption heat transformation, fresh water production from the air, adsorptive air-conditioning systems, etc.[1] Humidity-buffering materials are key components for water adsorption-desorption technologies. Various new compounds and materials for humidity-buffering materials have been reported in the past few decades, including zeolites, hydrophilic polymers, silica gel, activated carbon, aluminosilicate materials, biomass-based materials, metal-organic frameworks (MOFs), diatomite materials, and so forth.[2] Among them, porous humidity-buffering materials have attracted plenty of attentions because of their high surface areas, ordered pore distributions, good surface chemistry and high pore volumes.[3]

As is well known, small-sized inorganic nanocrystals with large specific surface areas have got extensive research interests owing to the possibility of tuning their optical, chemical and electronic property on a large scale, which can cause the tunable multi-functionalities.[4] α-Fe_2O_3, as the most stable iron oxide under ambient atmosphere, has sparked increasing interest over the past few decades because of its low cost, high corrosion resistance, abundant and eco-friendly properties.[5] To our knowledge, the potential application of α-Fe_2O_3 porous nanomaterials as a stand-alone material for adsorbents has not been studied yet. Herein, preparation and water vapour adsorption-desorption property of the well-dispersed α-Fe_2O_3 nanocubes in a narrow size distribution and large specific surface area are our main objectives. Nanoparticles exhibit properties different from those of their bulk counterparts, which can be exploited to obtain new functionalities.[6]

In this work, we presented a facile and simple one-pot hydrothermal approach to prepare α-Fe_2O_3 nanocubes with an average pore size distribution of 8.48 nm. The size of the nanocube is around 40-50 nm. The uniform ordered cube-like Fe_2O_3 nanomaterial showed an excellent humidity-buffering ability, due to adsorption and desorption of water vapour by utilizing the intra- and inter-granular pores and large specific surface areas. Specifically, the Fe_2O_3 nanocubes has a much higher water adsorption capacity compared with bulk Fe_2O_3 counterparts and porous Fe_2O_3 nanofibers. Further comparasion with the conventional humidity-buffering materials (raw diatomite and calcined diatomite) was conducted. Results show that the significantly enhanced water adsorption capacity of Fe_2O_3 nanocubes mainly arises from the appropriate pore size distribution nearby condensation critical radius.

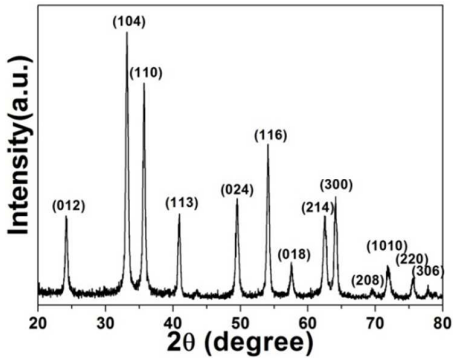

Fig. 1 XRD pattern of the as-synthesized Fe_2O_3 nanocubes.

[a] Key Laboratory for Anisotropy and Texture of Materials (Ministry of Education), Northeastern University, Shenyang 110819, China. Tel: 0086-24-83691565; E-mail: qingw@smm.neu.edu.cn
[b] State Key Laboratory of Rare Earth Resource Utilization, Changchun Institute of Applied Chemistry, Chinese Academy of Sciences, Changchun 130022, China

Electronic Supplementary Information (ESI) available: details of experimental procedures; XRD and SEM image of the bulk Fe_2O_3 powder and porous Fe_2O_3 nanofibers; SEM images of the Fe_2O_3 samples with different amounts of urea; SEM images of products prepared under similar conditions but with DEG replaced by EG, and PEG 400; N_2 adsorption-desorption isotherm for the conventional samples (raw diatomite and calcined diatomite). The inset shows BJH pore size distributions of the samples; Water sorption kinetics of the conventional samples (raw diatomite and calcined diatomite) equilibrated for a fixed time at room temperature. See DOI: 10.1039/x0xx00000x

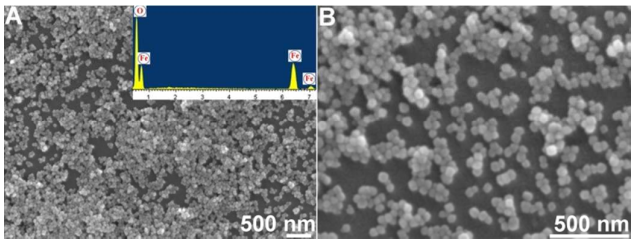

Fig. 2 (A) Low-magnification SEM image of the Fe_2O_3 nanocubes, and the EDS pattern (inset); (B) Enlarged SEM image of the Fe_2O_3 nanocubes.

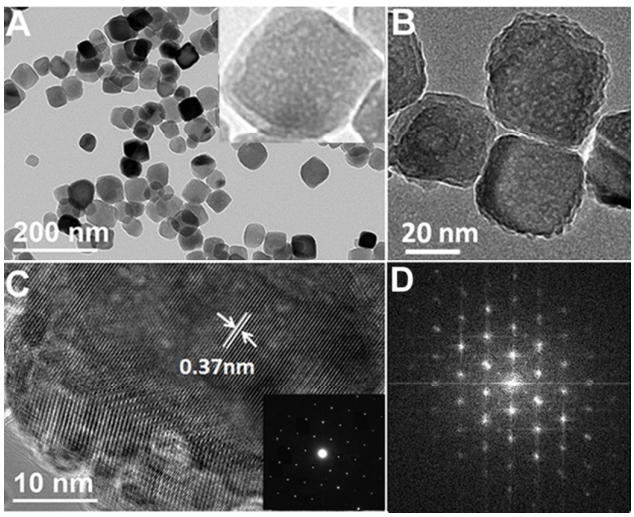

Fig. 3 (A) Low-magnification TEM image of the Fe_2O_3 nanocubes, inset shows a magnified nanocube to emphasize the internal nanoporosity; (B) Enlarged TEM image of the Fe_2O_3 nanocubes; (C) HR-TEM image and SAED pattern (inset) of the nanocubes. (D) FFT pattern of the edge area of nanocubes.

The structure and composition of the as-prepared powder samples was characterized by XRD analysis, as shown in Fig. 1. All the diffraction peaks can be identified to the Fe_2O_3 phase (JCPDS Card No. 33-0664). No other characteristic peaks from the other crystalline impurities were detected, thus indicating formation of the pure Fe_2O_3 products. The morphology and size of the as-prepared Fe_2O_3 products were visualized by SEM. The low-magnification SEM image (Fig. 2A) shows that the product is composed of uniform ordered nanocubes. The high-magnification SEM image (Fig. 2B) clearly reveal that, the cube-like shape have a narrow size distribution of 40-50 nm. Additionally, the chemical composition of these nanocubes is further investigated by energy-dispersive spectroscopy (EDS, inset in Fig. 2A). The strong peaks of Fe and O are observed in the EDS result, and the atomic percentage ratio is about 2:3, which is close to the stoichiometry of Fe_2O_3. For comparison, bulk counterpart Fe_2O_3 powder and Fe_2O_3 porous nanofibers were also measured.[7] The structure and morphology results were shown in Fig. S1. Pure Fe_2O_3 crystalline phases (JCPDS Card No. 33-0664) were identified. The morphology of commercial Fe_2O_3 powder was nanocables with particles, of which average particle size was about 100 nm. The morphology of uniform Fe_2O_3 porous nanofibers can be observed obviously.

Further insight into the microstructure and morphology of cubelike Fe_2O_3 nanoarchitecture was obtained through TEM and HR-TEM. Fig. 3A shows the low-magnification TEM images of the Fe_2O_3 nanostructures, uniform ordered small-sized nanocubes can be observed clearly, in accordance with the SEM results (such as Fig. 2B). The high-magnification TEM images in inset of Fig. 3A and Fig. 3B reveal the presence of mesopores in the nanocubes. The HR-TEM image (Fig. 3C), SAED (inset) and FFT pattern (Fig. 3D) exhibit the high-crystalline characterization with a lattice spacing of 0.37 nm, which can be indexed readily to (101) plane of Fe_2O_3 nanocubes.

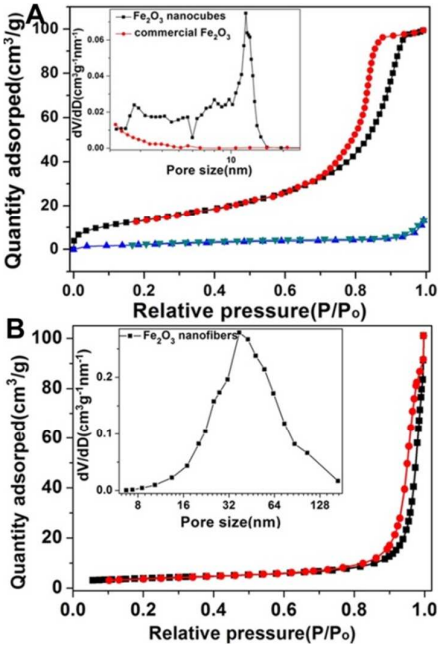

Fig. 4 N_2 adsorption-desorption isotherm for (A) the Fe_2O_3 nanocubes, bulk Fe_2O_3 and (B) Fe_2O_3 nanofibers. The inset shows BJH pore size distributions of the samples.

The specific surface area and porosity of the Fe_2O_3 samples were investigated. Fig. 4 shows the N_2 adsorption/desorption isotherms and Barret–Joyner–Halenda (BJH) pore size distribution curve of the as-obtained Fe_2O_3 naocubes, nanofibers and bulk Fe_2O_3 counterpart powder. Results show that the isotherm of Fe_2O_3 nanocubes can be categorized as type IV, with the distinct hysteresis loop observed in the range of 0.5-1.0 P/P_0 on the basis of IUPAC classification. Evidently, the pore size distribution is relatively narrow, with an average size of 8.48 nm. This result coincides with that of the TEM (Fig. 3A, B). The BET surface area and pore volume of Fe_2O_3 nanocubes are calculated to be 50.91 m^2/g and 0.17 cm^3/g respectively, which are much higher than that of bulk Fe_2O_3 counterpart powder (8.79 m^2/g, 0.02 cm^3/g) and porous Fe_2O_3 nanofibers (13.4 m^2/g, 0.15 cm^3/g).

Such a high specific surface area is believed to benefit from the synthesis process of nanocubes.[8] Control experiments were carried

out to determine the systhesis parameters that may affect the formation of Fe_2O_3 nanocubes. We found that the addition of urea and DEG has strong effects on the formation of nanocubes. Fig.S2 shows SEM images of the samples obtained when different amounts of urea are introduced into the reaction system. Without using urea, microrods with lengths of about 10 μm are the dominant products in the batch solution. Increasing the amount of urea, more and more nanocubes appear in the product together with a decreased amount of rod-like microstructures. The major role of urea can be assigned to provide OH^- ion supply in aqueous solution through $CO(NH_2)_2$ hydrolysis.[9] Fig. S3 gives SEM images of the products obtained when EG and PEG 400 replace DEG while keeping the other conditions unchanged. It is obvious that nanocubes can be fabricated only under the presence of DEG. As reported in literature, DEG with its high boiling point and viscosity property has been widely used in the polyol method to fabricate a series of monodisperse nanostructured materials.[10]

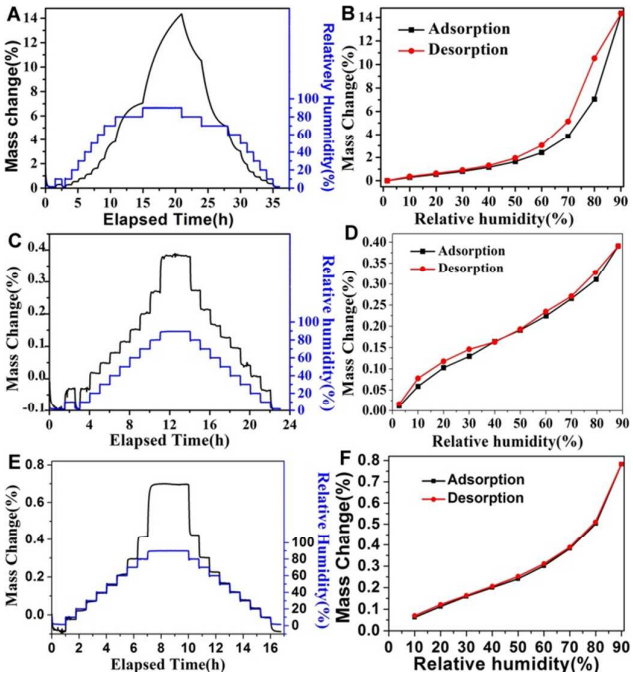

Fig. 5 Water adsorption-desorption kinetics and isotherms at room temperature of the Fe_2O_3 nanocubes (A,B), bulk Fe_2O_3 (C,D) and Fe_2O_3 nanofibers (E,F) samples equilibrated for a fixed time.

Comparative experiments were carried out to examine the effect of Fe_2O_3 nanomaterials on the water vapour adsorption-desorption. As shown in Fig. 5, the adsorption capacity of water vapour at both low and high humidity ranges follows the order of bulk Fe_2O_3 < Fe_2O_3 nanofibers < Fe_2O_3 nanocubes. This result is consistent with the trend of pore size, pore volume and surface area of Fe_2O_3 nanomaterials. In addition, conventional humidity-buffering materials (raw diatomite and calcined diatomite) were prepared and used as control samples. Their N_2 sorption isotherm, BJH pore size distribution and water sorption kinetic are shown in Fig. S4 and S5. The results of BET surface areas, BJH average pore sizes, pore volumes values and the maximum adsorption capacity of water vapor of the Fe_2O_3 nanocubes, Fe_2O_3 porous nanofibers, bulk Fe_2O_3 counterparts, raw diatomite and calcined diatomite samples were summarized in Table 1. The adsorption capacity of the Fe_2O_3 nanocubes was higher than that **of** the raw and calcined diatomites adsorbents. More interesting, similar BET surface areas were observed between the Fe_2O_3 nanocubes and calcined diatomite sample, but the water adsorption capacity of Fe_2O_3 nanocubes was found to be much higher than that of calcined diatomites adsorbent. In general, BET surface area is one of the most critical influences on water vapour adsorption performance.[11] Our experimental results demonstrate that there are some other influences on the water vapor adsorption efficiency, besides BET surface area in this system.[12] Considering the samples with different pore structure, pore size may be another big factors influencing their water vapour adsorption performance. For Fe_2O_3 nanocubes, the largest increase in uptake takes place in the range of medium RHs when the filling of micropores starts, and follows at the higher RHs by capillary condensation in the mesopores. At the relatively low water vapour pressure, the water is preferentially adsorbed on the highly hydrophilic sites, formed monolayer adsorption.[13] At the relatively higher pressure, multilayer adsorption occurs, followed by capillary condensation in the porous channels.[14]

Table 1 BET surface areas, BJH average pore sizes, pore volumes and maximum water adsorption capacity values of Fe_2O_3 nanocubes, Fe_2O_3 nanofibers, bulk Fe_2O_3 counterparts, raw diatomites and calcined diatomites.

Sample	Surface area (m^2g^{-1})	Pore size (nm)	Pore volume (cm^3g^{-1})	Max water sorption capacity (%)
Fe_2O_3 nanocubes	50.91	8.48	0.17	14
Fe_2O_3 nanofibers	13.4	35.2	0.15	0.8
Bulk Fe_2O_3	8.79	6.78	0.02	0.4
Raw diatomite	71.57	9.32	0.10	10
Calcined diatomite	52.45	6.75	0.09	6.4

For the capillary condensation phenomena, Kelvin equation can be used. At the higher RH, the pore diameter, where capillary condensation takes place, can be calculated *via* Kelvin equation:

$$\ln\left(\frac{p}{p_0}\right) = -\frac{2\sigma V_L}{\gamma_m RT}$$

where p is the vapor partial pressure; p_0 is the saturated vapour pressure; σ is the surface tension, V_L is the molar volume of the liquid, R is the universal gas constant (8.314 J/mol• K), γ_m is the Kelvin radius of the mesopores, and T is Kelvin's temperature. Corresponds to the capillary condensation, the saturation takes place in all the pores when radii is up to γ_m, under a constant pressure and temperature. Considering multi-layer adsorption, the respective average pore diameter for 75% humidity, using the corrected Kelvin equation, is about 8.5 nm (At this condition, the pore diameter for 75% humidity is about 8.5 nm). Therefore,

capillary condensation can be observed in the as-prepared Fe_2O_3 nanocubes with an average pore diameters of 8.48 nm. It means that the excellent humidity sensitivity obtained for the uniform Fe_2O_3 nanocubes can be explained by the favorable pore size distribution nearby condensation critical radius. Additionally, from the point of the irreversible chemisorption and reversible physisorption, this water vapour adsorption-desorption of Fe_2O_3 nanocubes is physisorption, due to the high stability of the water vapor adsorption-desorption capacity (Fig. 6).[15] Hence, the difference of water vapour adsorption of the samples was mainly dependent on the pore structures rather than surface chemical properties since many suspended oxygen bonds exist in this case.[16] Although further investigation is necessary to elucidate the water absorption-desorption mechanism of Fe_2O_3 nanocubes, we hope the present study will stimulate new investigations of the relationship between nanostructure materials and water vapour adsorption-desorption.

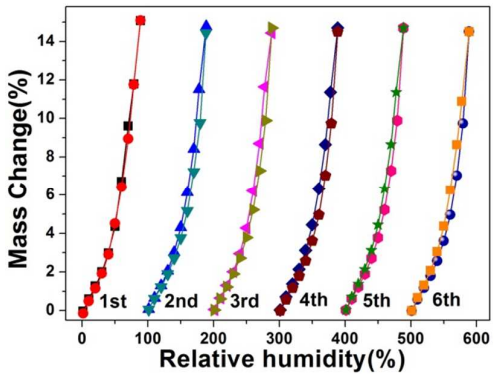

Fig. 6 Cycling runs for the water vapour adsorption-desorption over Fe_2O_3 nanocubes at room temperature.

Conclusions

In summary, we have successfully demonstrated Fe_2O_3 nanocubes with an average pore size distribution of 8.48 nm exhibits excellent humidity-buffering ability for the first time. The as-synthesized Fe_2O_3 nanocube samples show much higher water vapour adsorption/desorption performance than bulk Fe_2O_3 counterparts, porous Fe_2O_3 nanofibers and conventional humidity-buffering materials (raw and calcined diatomites). The superior water adsorption/desorption performance of Fe_2O_3 nanocubes can be attributed to the favorable pore size distribution around condensation critical radius. The present work might open new doors for the exploration of uniform ordered nanomaterials with excellent water vapour adsorption/desorption ability.

Notes and references

‡ The work was grateful to the financial aid from NSFC (51402047 and 5152500382), the Fundamental Research Funds for the Central Universities (N130410002), Doctoral Program of Higher Education of China (20130042120011), Open Project of State Key Laboratory of Rare Earth Resource Utilizations (RERU2014002).

1 (a) O. F. Osanyintola and C. J. Simonson, *Energ. Buildings,* 2006, **38,** 1270; (b) M. Woloszyn, T. Kalamees, M. O. Abadie, M. Steeman, A. S. Kalagasidis, *Build. Environ.,* 2009, **44**, 515.

2 (a) Y. K. Seo, J. W. Yoon, J. S. Lee, Y. K. Hwang, C. H. Jun, J. S. Chang, S. Wuttke, P. Bazin, A. Vimont, M. Daturi, S. Bourrelly, P. L. Llewellyn, P. Horcajada, C. Serre, G. Ferey, *Adv. Mater,* 2012, **24**, 806; (b) D. H. Vu, K. S. Wang, B. H. Bac, B. X. Nam, *Constr. Build. Mater.,* 2013, **38**, 1066; (c) X. L. Wei, W. L. Wang, J. Xiao, L. Zhang, H. Y. Chen, J. Ding, *Chem. Eng. J.,* 2013, **228**, 1133.

3 S. K. Seshadri, Y. S. Lin, *Sep. Purif. Technol.,* 2011, **76**, 261.

4 (a) H. D. Yu, M. D. Regulacio, E. Ye, M. Y. Han, *Chem. Soc. Rev.* 2013, **42**, 6006; (b) L. L. Geng, X. Y. Zhang, W. X. Zhang, M. J. Jia, G. Liu, *Chem. Commun.,* 2014, **50**, 2965.

5 (a) M. D. Hernández-Alonso, F. Fresno, S. Suárez, J. M. Coronado, *Energy Environ. Sci.,* 2009, **2**, 1231; (b) Y. Ye, C. Jo, I. Jeong, J. Lee, *Nanoscale*, 2013, **5**, 4584; (c) X. B. Chen, C. Li, M. Grätzel, R. Kostecki, S. S. Mao, *Chem. Soc. Rev.* 2012, **41**, 7909; (d) Y. J. Wang, Q. S. Wang, X. Y. Zhan, F. M. Wang, M. Safdar, J. He, *Nanoscale.* 2013, **5**, 8326; (e) M. T. Mayer, Y. J. Lin, G. B. Yuan, D. W. Wang. *Acc. Chem. Res.,* 2013, **46**, 1558; (f) X. Y. Meng, G. W. Qin, W. A. Goddard, S. Li, H. J. Pan, X. H. Wen, Y. K. Qin, L. Zuo, *J. Phys. Chem.,* 2013, **117**, 3779.

6 (a) K. Sivula, R. Zboril, F. L. Formal, R. Robert, A. Weidenkaff, J. Tucek, J. Frydrych, and M. Grätzel, *J. Am. Chem. Soc.,* 2010,**132**, 7436; (b) X. L. Hu, J. C. Yu, J. M. Gong, Q. Li, G. S. Li, *Adv. Mater.,* 2007, **19**, 2324; (c) J. Qu, Y. Yu, C. Y. Cao, W. G. Song, *Chem. Eur. J.* 2013, **19**, 11172; (d) L. Xu, J. X. Xia, L. G. Wang, J. Qian, H. M. Li, K. Wang, K. Y. Sun, M. Q. He, *Chem. Eur. J.* 2014, **20**, 2244.

7 (a) J. Sundaramurthy, P. Suresh Kumar, M. Kalaivani, V. Thavasi, S. G. Mhaisalkara, S. Ramakrishna, *RSC Adv.,* 2012, **2**, 8201; (b) J. Wu, N. Wang, L. Wang, H. Dong, Y. Zhao, L. Jiang, *ACS Appl. Mater. Interfaces* 2012, **4**, 3207.

8 (a) Z. H. Wei, R. G. Xing, X. Zhang, S. Liu, H.H. Yu, P. C. Li, *ACS Appl. Mater. Interfaces* 2013, 5, 598; (b) H. J. Wang, J. Gao, Z. G. Li, Y. L. Ge, K. Kan, K. Y. Shi, *CrystEngComm,* 2012, **14**, 6843.

9 (a) L. P. Zhu, N. C. Bing, L. L. Wang, H. Y. Jin, G. H. Liao, L. J. Wang, *Dalton Trans.*, 2012, **41**, 2959; (b) S. Y. Ho, A. S. W. Wong, G. W. Ho, *Cryst. Growth Des.,* 2009, **9**, 732.

10 F. Cao, D. Q. Wang, R. P. Deng, J. K. Tang, S. Y. Song, Y. Q. Lei, S. Wang, S. Q. Su, X. G. Yang, H. H. Zhang, CrystEngComm, 2011, 13, 2123.

11 (a) M. N. Golubovic, H. D. M. Hettiarachchi, W. M. Worek, *Int. J. Heat Mass Transf.,* 2006, **49**, 2802; (b) H. Desmorieux, N. Decaen, *J. Food Eng.,* 2006, **77**, 64.

12 (a) K. W. Liu, M. Sakurai , M. Aono, *Small,* 2012, **8**, 23, 3599; (b) M. Sheng, L. L. Gub, R. Kontica, Y. Zhou, K. B. Zheng, G. R. Chen, X. L. Mo, G. R. Patzke, *Sens. Actuators B,* 2012, **166-167**, 642.

13 X. Li, Z. Li, J. *Chem. Eng. Data,* 2010, **55**, 5729.

14 F. S. Tsai, S. J. Wang, *Sens. Actuators B,* 2014, **193**, 280.

15 H. B. Li, M. H. Ai, B. Z. Liu, S. J. Zheng, G. Q. Zong, *Micropor. Mesopor. Mater.,* 2011, **143**, 1.

16 (a) X. Li, Z. Li, Q. B. Xia, H. X. Xi, *Appl. Therm. Eng.,* 2007, **27**, 869; (b) Z. Li, H. Zhang, W. Zheng, W. Wang, H. Huang, C. Wang, A. G. MacDiarmid, Y. Wei, *J. Am. Chem. Soc.,* 2008, **130**, 5036.